

Photochemical processes drive thermal responses of dissolved organic matter in the dark ocean

Ang Hu^{1,2}, Yifan Cui^{1,2}, Sarah Bercovici^{3,4}, Andrew J. Tanentzap⁵, Jay T. Lennon⁶, Xiaopei Lin⁷, Yuanhe Yang⁸, Yongqin Liu⁹, Helena Osterholz¹⁰, Hailiang Dong¹¹, Yahai Lu¹², Nianzhi Jiao¹³, Jianjun Wang^{1,2,*}

¹ Key Laboratory of Lake and Watershed Science for Water Security, Nanjing Institute of Geography and Limnology, Chinese Academy of Sciences, Nanjing, China

² State Key Laboratory of Lake Science and Environment, Nanjing Institute of Geography and Limnology, Chinese Academy of Sciences, Nanjing, China

³ Institute for Chemistry and Biology of the Marine Environment (ICBM), University of Oldenburg, Oldenburg, Germany

⁴ National Oceanography Centre, Southampton SO14 3ZH Hampshire, United Kingdom

⁵ Ecosystems and Global Change Group, School of the Environment, Trent University, Peterborough, Canada

⁶ Department of Biology, Indiana University, Bloomington IN 47405, USA

⁷ Frontier Science Center for Deep Ocean Multispheres and Earth System (FDOMES) and Physical Oceanography Laboratory, Ocean University of China, Qingdao, China

⁸ State Key Laboratory of Vegetation and Environmental Change, Institute of Botany, Chinese Academy of Sciences, Beijing, China

⁹ Center for the Pan-third Pole Environment, Lanzhou University, Lanzhou, China

¹⁰ Marine Chemistry, Leibniz Institute for Baltic Sea Research Warnemünde, Rostock, Germany

¹¹ State Key Laboratory of Biogeology and Environmental Geology, China University of Geosciences, Beijing, China

¹² College of Urban and Environmental Sciences, Peking University, Beijing, China

¹³ Innovation Research Center for Carbon Neutralization, Fujian Key Laboratory of Marine Carbon Sequestration, Xiamen University, Xiamen, China

* Correspondence: jjwang@niglas.ac.cn

Abstract

How dissolved organic matter (DOM) responds to climate warming is critical for understanding its effectiveness as a natural climate solution. Here, we use a highly resolved dataset of 821 DOM samples covering the surface waters to the deep Atlantic, Southern, and Pacific oceans to examine molecular-level responses to warming water temperatures, i.e. their thermal responses. In general, the strength and diversity of thermal responses among individual molecules both decline towards the deep waters, but they show decreasing and increasing trends with more recalcitrant molecules in concentration, respectively. Their contrasting trends concur with the more important role of photochemical processes in explaining the diversity of thermal responses than the strength. By projecting global ocean thermal responses from 1950-2020, we predict increases in the diversity are unexpectedly largest at deeper depths (> 1,000 m). Such increases could elevate recalcitrant deep-ocean carbon sink by approximately 10 Tg C yr⁻¹ which accounts for > 5% of the carbon flux survived to the deep ocean. Our findings highlight the importance of photochemical legacies in driving DOM thermal responses and further help predict the future oceanic carbon sink under global change.

Dissolved organic matter (DOM) in the ocean is one of the largest carbon reservoirs on Earth, holding ~660 petagrams of carbon—more carbon than marine and terrestrial biota combined (Hansell et al. 2009, Dittmar et al. 2021). Marine DOM responses to anthropogenic warming are crucial for understanding coupled global carbon stocks and Earth’s climate (Peltier et al. 2007, Sexton et al. 2011, Henson et al. 2022, Jiao et al. 2024). However, predicting how, and to what extent, marine DOM responds to climate change is challenging. Past studies have focused on coarse-level processes such as ecosystem-scale carbon fluxes (Middelburg et al. 1996, Wohlers et al. 2009, Lonborg et al. 2018), and the metabolic activities of microorganisms such as growth and respiration rates (Yvon-Durocher et al. 2012, Bendtsen et al. 2015), partially because DOM is challenging to assess analytically. DOM consists of thousands of individual organic molecules, each of which can respond differently to warming owing to their varying chemical properties (Hu et al. 2024) and these responses may be only observable over decades in the ocean (Lonborg et al. 2018). Therefore, resolving how individual molecules respond to warming can provide more accurate predictions of the fate of DOM than those based on ecosystem-level measurements.

The development of an indicator to predict the response of DOM to warming, i.e. its thermal response, is a recent advance in forecasting future changes of ecosystem-level carbon stocks (Hu et al. 2024). This indicator reflects the **collective** thermal responses of all the individual molecules in DOM and so can be used to estimate the extent to which carbon fluxes respond to future warming (Hu et al. 2024). For instance, the dominance of aliphatic and peptide-like molecules with positive thermal responses largely promotes carbon stocks in lake sediments under warmer temperatures (Hu et al. 2024). Overall, the indicator has a ‘strength’ dimension that quantifies the balance between negative and positive thermal responses among individual molecules, describing the magnitude of the dominant molecules’ changes with warming. The indicator also has a ‘diversity’ dimension that quantifies variability in molecule-level responses to temperature. This dimension captures unique chemical properties associated with complementary resources available to decomposers or abiotic processing that can synergistically influence carbon fluxes (Vos et al. 2013, Barantal et

al. 2014). Notably, the **novel ‘diversity’ dimension** of thermal responses and its influence on the DOM inventory, however, have been unexplored in previous studies.

The strength and diversity of thermal responses may be differentially driven by ecosystem processes affecting DOM turnover such as microbial and photochemical transformations. For example, microbial processing of DOM depends more deterministically on environmental conditions, such as higher temperatures that increase kinetic energy, enzymatic activities and primary productivity (Davidson and Janssens 2006, Toseland et al. 2013, Anderson et al. 2021, Hu et al. 2022). Additionally, enzymatic substrate specificity can increase the efficiency of microbial transformation of DOM by reducing the energetic and resource demands to maintain metabolic processes (Zakem et al. 2021, Hu et al. 2022). DOM assemblages structured by microbial processing should therefore be dominated by molecules with strong positive thermal responses at higher temperatures, that is, increased strength of thermal responses. In contrast, abiotically driven photochemical transformations of DOM are more stochastic and should depend less on environmental fluctuations. This is largely because the molecules with either high or low temperature sensitivities can be susceptible to photochemical processes. Moreover, DOM can be non-selectively photodegraded across a wider range of molecules via strong and abundant oxidizing agents, such as reactive oxygen species and radical intermediates (Cory and Kling 2018). DOM assemblages shaped by photochemical processes should therefore be composed of molecules with more variability in thermal responses, that is a higher diversity of thermal responses.

Here, we used a comprehensive global ocean dataset to examine the strength and diversity of thermal responses in DOM and the underlying ecosystem processes. DOM composition was measured with Fourier transform ion cyclotron resonance mass spectrometry (FT-ICR MS) in 821 samples from the entire water column across a 5,800 m depth gradient in the Atlantic, Southern, and Pacific oceans (Fig. S1) (Bercovici et al. 2023a). The strength and diversity of thermal responses for each sample were quantified based on the direction and magnitude of each molecular formula’s (hereafter molecule’s) thermal response, termed a molecule-specific environmental response to

temperature (MER) (Hu et al. 2024). The MER is defined as the effect size of changes in the relative abundance of each molecule as a function of water temperature across sites spanning broad geographical gradients. The abundance-weighted average of MERs in each DOM sample was then used to derive an indicator of the strength of thermal responses, termed the average of compositional-level environmental responses to temperature ($iCER_{avg}$). Low and high values of $iCER_{avg}$ reflect a DOM assemblage that is dominated by molecules that deplete and accumulate with warming temperatures, respectively (Hu et al. 2024). For the diversity of thermal responses, we calculated the abundance-weighted standard deviation of MERs in each DOM sample, termed $iCER_{var}$. Low values of $iCER_{var}$ reflect a DOM assemblage composed of molecules with similar MERs, while high values reflect a DOM assemblage of molecules with divergent MERs. With these new approaches, we addressed three main questions: (1) How do the molecular-level thermal responses of DOM vary among individual molecules and how are they associated with chemical properties? (2) How do the ecosystem-level thermal responses of DOM (i.e., $iCER_{avg}$ and $iCER_{var}$) vary along environmental and geographical gradients (latitude, water depth, and temperature)? and (3) How are these responses influenced by microbial versus photochemical processes? We then predict the spatiotemporal changes in $iCER_{avg}$ and $iCER_{var}$ in the global ocean and discuss how these responses might influence standing stocks of dissolved organic carbon (DOC) that play an important role in regulating the global climate.

Molecular-level thermal responses of DOM

In the Atlantic and Pacific oceans, DOM thermal responses varied substantially among individual molecules (Fig. 1a). Most molecules were significantly ($P \leq 0.05$) correlated in relative abundance with water temperature, with 38% ($n = 1,634$) showing negative responses and 36% ($n = 1,551$) showing positive responses (Fig. 1a). Across molecules, MER ranged from -0.72 to 0.83, with median values of -0.23 and 0.21 for negative and positive responses, respectively (Fig. 1a). Notably, the magnitudes and directions of negative, positive, and neutral thermal responses of individual molecules were generally consistent across spatial scales, such as between the Atlantic and Pacific

oceans (Fig. 1b) and across different cruises (Fig. S2). For instance, each molecule showed consistent MERs between the Atlantic and Pacific oceans, with high correlation (Pearson $r = 0.80$) and linear regression slope of 0.71 ($P \leq 0.001$; Fig. 1b). This strong spatial transferability of MERs was also true across different biochemically defined compound classes of DOM (Fig. 1b). Together, these results provide strong evidence that the responses of individual molecules to temperature change are transferable and generalizable across the global ocean.

The disparate thermal responses among individual DOM molecules could be explained in part by chemical traits, such as their recalcitrance and oxidation state (Figs. 1c-e). As MER became more positive, over 75% of warm-accumulating molecules were classed as aliphatic-like and highly unsaturated compounds with low oxygen content (Fig. 1c). These molecules were characterized by lower recalcitrance, indicated by an elevated H/C ratio and a lower aromaticity index (Figs. 1d, 1e). In contrast, as MER became more negative, warm-depleting molecules shifted towards highly unsaturated compounds with high oxygen content and higher recalcitrance, as indicated by a reduced H/C ratio from a mean of 1.25 to 1.08 and an increased aromaticity index from 0.23 to 0.32 (Figs. 1c-e). These molecules also had a relatively higher oxidation state as indicated by the reduction in Gibbs free energy from a mean of 69 to 58 kJ (mol C)⁻¹ and an increased O/C ratio from 0.43 to 0.53 (Figs. 1d, 1e).

We further found that the recalcitrant molecules with negative thermal responses were evenly distributed in concentration throughout the water column, suggesting they persisted across the global ocean (Figs. 2, S3, S4). For instance, the apparent carbon concentrations of individual molecules with negative MERs, quantified with their DOC-normalized peak intensities (Flerus et al. 2012, Bercovici et al. 2023b) (see Methods eq. 6), generally showed non-statistically significant changes with water depth at 82% of stations on average ($P > 0.05$; Fig. 2d). Similarly, few changes throughout the water column were observed in the composition and concentrations in molecular constituents, i.e. the bins of these molecules classified according to their MERs (see Methods; Figs. 2e, 2f). However, for individual molecules or the bins with more positive MERs, their apparent carbon concentrations decreased towards the deep ocean

(Figs. 2d-f, S3, S4). This pattern of the molecules with negative MERs aligns with the persistence concept of refractory DOC, which shows stable bulk carbon concentrations across water depths and may serve as an oceanic carbon sink (Beaupré and Aluwihare 2010, Hansell 2013). Furthermore, the degradation state index (I_{deg}) (Flerus et al. 2012) provides additional support for inferences about the persistence of molecules with negative thermal responses. At the molecular level, the apparent carbon concentrations of individual molecules or the bins with negative MERs generally showed few (less than 20% of stations on average) statistically significant changes with the I_{deg} ($P \leq 0.05$; Fig. S5). Rather, molecules accumulated with more degraded (i.e., older) DOM where they had more negative MERs, i.e. inverse relationship between the MER and the correlation coefficient between the relative abundance of each molecule and I_{deg} of the corresponding sample ($R^2 = 0.97$; $P \leq 0.001$; Fig. S6a). Likewise, at the compositional level, a more negative iCER_{avg} was strongly associated with older, more degraded DOM, as revealed by its inverse relationship with I_{deg} ($R^2 = 0.87$; $P \leq 0.001$; Fig. S6b).

DOM thermal responses across latitudes and water depths

We quantified the strength (iCER_{avg}) and diversity (iCER_{var}) of thermal responses for each DOM assemblage by aggregating individual molecules' MERs, and examined their geographical patterns. For the strength of thermal responses, iCER_{avg} ranged from -0.11 to 0.11, with a mean of -0.03, and significantly decreased towards higher absolute latitudes ($R^2 = 0.21$; $P < 0.001$; Fig. 3a). The associations between iCER_{avg} and absolute latitude varied across different water depths. The slopes of linear regressions were statistically negative ($P \leq 0.05$) at shallower depths (≤ 200 m) but not statistically significant ($P > 0.05$) at deeper depths (> 200 m) (Fig. S7).

Compared to the iCER_{avg} , the diversity iCER_{var} showed weaker latitudinal patterns (Figs. 3, S7). Specifically, iCER_{var} decreased towards higher absolute latitudes by a mean of only 1.7% as compared with a 1087.9% average change in iCER_{avg} (Fig. 3b). Across water depths, the linear slopes between iCER_{var} and absolute latitude were statistically negative ($P \leq 0.05$) at shallower depths (≤ 200 m), non-statistically significant ($P > 0.05$) at greater depths, and eventually statistically positive ($P \leq 0.05$)

at depths greater than 3,000 m (Figs. 3b, S7). In addition, $iCER_{avg}$ and $iCER_{var}$ both significantly decreased with depth ($R^2 = 0.22$ to 0.27 ; $P < 0.001$; Figs. 3c, d).

The observed geographical patterns suggest that temperature plays an important role in explaining both $iCER_{avg}$ and $iCER_{var}$. This is supported by the observation that both $iCER_{avg}$ and $iCER_{var}$ showed positive relationships with water temperatures, with R^2 of 0.54 and 0.30, respectively ($P < 0.001$; Figs. 3e, f). We further found that the slope of linear regression between $iCER_{avg}$ and temperature was highest in the 60-100 m water layers, increasing $iCER_{avg}$ of 0.0036 per 1 °C, while for $iCER_{var}$, the slope was greatest in the 300-1,000 m layers, increasing by 0.0016 per 1 °C ($P \leq 0.05$; Fig. S7). This result suggests that the highest sensitivity of thermal responses to warming occurs at shallower depths for the strength of thermal responses, but deeper depths for the diversity.

Implications of DOM thermal responses and underlying ecosystem processes

We found that the diversity of thermal responses was a better predictor of recalcitrant DOC concentration than the strength, which is especially true in the deep ocean. At shallower depths (≤ 200 m), both $iCER_{avg}$ and $iCER_{var}$ exhibited statistically positive relationships with DOC concentration, as well as with the apparent carbon concentrations of less recalcitrant molecules (that is, molecules with more positive MERs) ($P < 0.05$; Figs. 4a-d, S8, S9). However, at deeper depths ($> 1,000$ m), $iCER_{avg}$ and $iCER_{var}$ showed contrasting relationships with DOC concentration (Figs. 4a-d, S8). Specifically, $iCER_{avg}$ showed a marginally negative relationship with DOC ($R^2 = 0.03$; $P = 0.025$), while $iCER_{var}$ had a statistically positive relationship ($R^2 = 0.22$; $P < 0.001$; Figs. 4a, c). These contrasting patterns are in line with decreasing and increasing trends of $iCER_{avg}$ and $iCER_{var}$, respectively, with the apparent carbon concentrations of more recalcitrant molecules (that is, molecules with more negative MERs) (Figs. 4b, 4d, S9). Notably, the magnitude of trends for $iCER_{var}$ were larger than $iCER_{avg}$ (Figs. 4b, 4d, S9). For instance, as MER became more negative, the linear slopes between $iCER_{avg}$ and the apparent carbon concentrations of molecules with negative MERs, especially at depths of $> 1,000$ m, were generally negative and declined to -13, while for $iCER_{var}$,

the slopes were positive and increased to 54 (Figs. 4b, d). Collectively, these results indicate that more diverse responses to warming among individual molecules can result in higher concentrations of recalcitrant DOC.

The contrasting results between the strength and diversity of thermal responses could be explained by different ecosystem processes affecting DOM turnover. Microbial transformations and photochemical degradation are two key processes that control the production and consumption of DOM under specific environmental conditions such as temperature, salinity, and light (Mopper et al. 1991, Jiao et al. 2010, Dittmar et al. 2021, Bercovici et al. 2023c). The thermal responses of DOM are expected to be influenced directly by environmental factors and indirectly through the two ecosystem processes. For instance, environmental factors, such as water temperature, salinity, latitudes, and water depth, explained 52-67% of the variations in both $iCER_{avg}$ and $iCER_{var}$, except for $iCER_{avg}$ at deeper depths ($> 1,000$ m) with only 6% explained variation (Fig. S10). We then examined the effects of two processes which were quantified using the indices of I_{bio} and I_{photo} . These two indices are based on the relative abundance of ten marker molecules that estimate the contributions of microbially reworked and photochemically degraded DOM, respectively (Osterholz et al. 2015, Stubbins and Dittmar 2015, Bercovici et al. 2023c). High I_{bio} and low I_{photo} values indicate that biological reworking and photodegradation, respectively, have shaped the current DOM composition (Bercovici et al. 2023c).

Interestingly, photochemical degradation was more important in driving the diversity of thermal responses than the strength across both surface and deep waters. Specifically, the $iCER_{avg}$ had a much weaker relationship with I_{photo} ($R^2 = 0.11$; $P < 0.001$) compared to I_{bio} ($R^2 = 0.75$; $P < 0.001$; Fig. 4e). When accounting for the effects of environmental factors such as water temperature and salinity, I_{photo} had nearly half the magnitude of direct effects on $iCER_{avg}$ (mean standardized effect = 0.37; $P \leq 0.001$) compared to I_{bio} (mean effect = 0.77; $P \leq 0.001$; Fig. 4f). In contrast, the $iCER_{var}$ depended more on photodegradation than microbial transformations. The $iCER_{var}$ strongly declined with I_{photo} ($R^2 = 0.67$; $P < 0.001$), but had a weaker relationship with I_{bio} ($R^2 = 0.39$; $P < 0.001$), indicating that stronger photodegradation results in higher

iCER_{var} (Fig. 4g). Even when accounting for the influences of environmental factors, the dominant effects of I_{photo} on iCER_{var} remained, with I_{photo} having 2.5 times the direct effects compared to I_{bio} (mean standardized effect = -0.72; $P \leq 0.001$ vs. mean effect = 0.29; $P \leq 0.001$; Fig. 4h). The dominant effects of I_{photo} on iCER_{var} were maintained across both shallower and deeper depths (Figs. 4g, h).

The above results indicate that photochemical processes could leave pronounced legacy effects on the deep ocean and contribute to the persistence of DOM. This seems counterintuitive because photodegradation generally occurs in the surface layer with high solar radiation and the generation of reactive oxygen species (Mopper et al. 2015, Wagner et al. 2020). The only possible explanation is that nonselective photodegradation produces a wider range of DOM molecules with diverse molecular properties (Cory and Kling 2018) and the partially photodegraded DOM likely escapes from microbial action upon export out of the euphotic zone and can persist down to deeper waters (Sofianos and Johns 2007, Cory et al. 2014, Bercovici et al. 2023c). The exported photochemical DOM could elevate the diversity of thermal responses and the persistence in the deep ocean, that is, legacy effects of photochemical processes. In contrast, microbially transformed DOM produced in the surface waters could hardly reach the deep ocean due to the long journey of remineralization (Dall'Olmo et al. 2016, Bercovici et al. 2023c). This explanation could be further supported by the DOM molecular traits in the deep waters. Only at deeper depths (> 1,000 m), iCER_{var} increased with molecular recalcitrance indicated by a reduced H/C ratio or an elevated aromaticity index ($R^2 = 0.11$ to 0.28 ; $P < 0.001$; Fig. S11). However, iCER_{avg} positively correlated across both shallower and deeper depths with molecular lability indicated by elevated H/C ratio or Gibbs free energy ($R^2 = 0.88$ to 0.94 ; $P < 0.001$; Fig. S11).

Predicting DOM thermal responses and carbon sink changes in the global ocean

We found that environmental variables can predict the spatiotemporal changes in the strength and diversity of thermal responses across the global ocean (Fig. 5, Table S3). We trained a machine learning model – random forest (Breiman 2001) – to identify the variables that best explained iCER_{avg} and iCER_{var}. We analyzed 13 environmental

variables, including water depth, the mean and seasonality of ocean temperature, salinity, and radiation attributes (see Methods). Ocean temperature was most important for predicting $iCER_{avg}$, while other variables were relatively unimportant (Fig. 5a). For $iCER_{var}$, however, the most important variable was ocean temperature, followed by salinity, water depth, and the seasonalities of temperature, salinity, and surface sensible heat flux (Fig. 5b). Overall, the environmental variables explained 70% and 62% of the variation in $iCER_{avg}$ and $iCER_{var}$, respectively (Figs. 5a, b).

The projected strength and diversity of thermal responses both declined towards the deep waters and showed less latitudinal variations in the deep ocean. In general, the global mean (\pm SD) thermal responses in 2020 were -0.051 (± 0.020) for $iCER_{avg}$ and 0.399 (± 0.006) for $iCER_{var}$ (Figs. 5c, 5d, S12). Towards greater water depths, the mean $iCER_{avg}$ and $iCER_{var}$ both declined from the surface until becoming practically invariant below $\sim 1,000$ m, though the decline in $iCER_{var}$ was more gradual (Figs. 5e, f). At shallower depths ($< 1,000$ m), $iCER_{avg}$ and $iCER_{var}$ peaked in the subtropical oceans roughly between 20° and 40° , while at deeper depths ($> 1,000$ m), they were relatively low and more evenly distributed across latitudes (Figs. 5c-f, S12). Both thermal responses were highest in subtropical shallower waters ($< 1,000$ m) likely because of high microbial and photochemical transformation and export of primary production to the DOM pool in subtropical gyres (Emerson et al. 1997, Schlitzer 2004, Toseland et al. 2013, Roshan and DeVries 2017).

Since 1950, the deep ocean has generally experienced greater increases in the diversity of thermal responses compared to the strength. Specifically, the global mean (\pm SD) increases in $iCER_{avg}$ and $iCER_{var}$ from 1950 to 2020 were 0.922% (± 1.622) and 0.028% (± 0.028), respectively (Figs. 5g, h). Along the surface-to-deep-ocean gradient, $iCER_{avg}$ and $iCER_{var}$ exhibited significant temporal changes at over 95% of depths, most of which were positive at 72% and 85% of depths, respectively (Figs. 5g, 5h, S13). The largest temporal changes occurred at different water depths between $iCER_{avg}$ and $iCER_{var}$. For $iCER_{avg}$, the temporal changes were generally positive and large at shallower depths, with a maximum of 6.942% at 81 m, then sharply diminishing to zero and eventually becoming negative at deeper depths ($> 1,457$ m). In contrast, the

temporal changes in $iCER_{var}$ were negative only at shallower depths (0-283 m) but remained positive afterwards, with a maximum of 0.063% at 1,401 m (Figs. 5g, h). The greater increases in $iCER_{var}$ compared to $iCER_{avg}$ in the deep ocean were further supported by the overall increase in their temporal changes. For instance, at depths of > 1,000 m, the temporal changes in $iCER_{avg}$ were almost negligible with a net increase of 0.005%, but the net increase in $iCER_{var}$ was ten times higher (0.047%) (Figs. 5g, h). Notably, the water temperature from 1950 to 2020 increased by an average of only 0.07 (± 0.08) °C at deeper depths below 1,000 m versus 0.68 (± 0.51) °C at 1 m depth (Fig. S14). The unexpected and substantial increases in the diversity of thermal responses is thus contrasting with the relatively stable environments such as water temperature in the deep ocean, and could have important ecological consequences.

The above findings have far-reaching implications for the future of deep-ocean carbon sink under global change. This is largely because the diversity of thermal responses was strongly positively correlated with recalcitrant DOC especially in the deep ocean (Fig. 4). For instance, at deeper depths (> 1,000 m), changes in the diversity of thermal responses from 1950 to 2020 alone could elevate the apparent concentrations of recalcitrant DOC (i.e., molecules with negative MERs) by 9.87 (± 3.35) Tg C yr⁻¹ (Table S3; see Methods). This increase in recalcitrant DOC, primarily formed by abiotic photochemical processes, could account for at least 5% of the DOC fluxes survived to the deep ocean, given that ~ 200 Tg C yr⁻¹ of DOC is exported from the euphotic zone to depths > 500 m (Hansell et al. 2009). This increase is important for the deep-ocean carbon sink considering there is no net increase of sediment carbon storage in the open ocean since the industrial revolution (Regnier et al. 2022). As the deep ocean stores about 72% of the global DOC inventory for years to centuries (Hansell et al. 2009), future ocean warming will substantially accelerate the accumulation of more persistent DOM in the deep ocean. This estimate is, however, caveated by several uncertainties. For instance, the deep-ocean carbon sink could be influenced by other potential important factors, but not considered here, such as dilution effects of labile DOC with low concentrations (Arrieta et al. 2015), and the inputs of recalcitrant DOC from ancient deposits or hydrothermal circulation (McCarthy et al. 2011, Wagner et al. 2020, Dittmar

et al. 2021). Nevertheless, our estimate emphasizes the pivotal but overlooked links between the diversity of thermal responses and both the magnitude and persistence of the global oceanic carbon sink. Collectively, our findings suggest that the role of the deep ocean as a global carbon sink will be amplified in the future because of increasing diversity in the thermal responses of DOM.

In conclusion, our study provides insights into how, and to what extent, oceanic DOM responds to climate warming considering the strength and diversity of thermal responses among individual molecules. The findings indicate that the diversity of thermal responses may be a better predictor of recalcitrant DOC concentrations than the strength. The deep ocean, conventionally considered a quasi-steady environment, has experienced an increasing diversity of thermal responses since 1950. This increase corresponds to an accumulation of approximately 10 Tg C yr^{-1} in recalcitrant deep-ocean carbon sink, mainly owing to the legacy effects of photochemical processes. Our results imply that the diversity of thermal responses in the deep ocean is sensitive to a warmer climate and could act as a negative feedback mechanism in the future, which needs to be taken into account in future predictive models or in ocean carbon budgets (Armstrong McKay et al. 2021, Friedlingstein et al. 2023). Future insights into the synergistic effects of photochemically driven carbon sequestration and other mechanisms, such as biological carbon pump (Jiao et al. 2024), would enhance our understanding of carbon sequestration, contribute to combating climate change, and improve projections of future ocean carbon storage.

Methods

Sample collection

To examine the responses of dissolved organic matter (DOM) to temperature change, we used a global ocean dataset spanning broad geographical gradients. The *in situ* long-term processes structuring DOM under climate change can be well captured using a space-for-time substitution derived from sampling sites with different temperatures along geographical gradients (Pickett 1989). A total of 821 samples for DOM composition were collected from 124 stations, covering the entire water column across depth gradients from 5 to 5,874 m during six research cruises in the Atlantic, Southern, and Pacific oceans (Fig. S1). Samples were collected during three *R.V. Polarstern* cruises ANT-XXVIII/2, ANT-XXVIII/4 and ANT-XXVIII/5 in austral spring and summer (Dec 2011 - May 2012) for the Atlantic and Southern Oceans, and three *R.V. Sonne* cruises SO245 (December 2015 to January 2016), SO248 (May 2016) and SO254 (January and February 2017) for the Pacific Ocean (Fig. S1). These cruises spanned latitudinal transects from 70.5°S to 43°N in the Atlantic and Southern Oceans and from 52°S to 59°N in the Pacific Ocean. For simplicity, we categorized the samples as Atlantic and Pacific Ocean, with the “Atlantic” group including the Atlantic and Southern Ocean samples. All samples were collected from a rosette of Niskin samplers. In addition, environmental variables such as water temperature and salinity were assessed. For further details of sampling, cruise track, location of stations, and environmental variable measurement in the Atlantic and Pacific Oceans see Bercovici et al. (2023a) and Bercovici et al. (2023c).

FT-ICR MS analysis of DOM samples

DOM of water samples was solid-phase extracted (SPE) for Fourier-transform ion cyclotron resonance mass spectrometry (FT-ICR MS) measurement (Dittmar et al. 2008). Briefly, 4 L of seawater were filtered through a pre-combusted (400 °C, 4 h) 0.7-µm glass fiber filters (GF/F, Whatman, United Kingdom), and the filtered water was acidified to pH 2 using 25% HCl and further extracted using 1 g PPL cartridges (Agilent Technologies). Cartridges were rinsed with pH 2 ultrapure water and dried with N₂ gas.

The DOM was then eluted with 6 ml of methanol (HPLC-MS grade) into pre-combusted amber glass vials and immediately stored at -20 °C until FT-ICR MS analysis. The SPE-DOC concentrations were analyzed on a Shimadzu TOC-VPCH total organic carbon analyzer. Detailed method of DOM extraction has been previously described (Bercovici et al. 2023c).

Highly accurate mass measurements of DOM extracts were conducted using FT-ICR MS (solarix XR™ system, Bruker Daltonik GmbH, Bremen, Germany) equipped with a 15 Tesla superconducting magnet and a standard electrospray ionization (ESI) interface (Apollo II, Bruker Daltonics). For FT-ICR MS analysis, the extracts were mixed with methanol and ultrapure water (MS grade, 1:1 v/v) to a final carbon concentration of 2.5 mg C L⁻¹ immediately preceding FT-ICR MS analysis. For analysis validation, an in-house DOM reference sample, collected at the Natural Energy Laboratory of Hawaii Authority in 2009 (Green et al. 2014), was measured regularly. FT-ICR-MS measurements were conducted in ESI negative ion mode, following the same method described in Bercovici et al. (2022).

Molecular composition and characteristics of DOM

In total, 6,114 peaks had formula assignments for 821 samples and these formulae are referred to as “molecules” throughout the manuscript. The **relative abundance** (or intensity) of molecules was calculated by normalizing signal intensity of each peak to the sum of all assigned intensities within each sample. These molecules were categorized into seven compound classes based on van Krevelen diagrams (Kim et al. 2003) and modified aromaticity index (AI_{mod}) (Spencer et al. 2014, Koch and Dittmar 2016). The compound classes were defined as follows: low O unsaturated (AI_{mod} < 0.5, H/C < 1.5, O/C < 0.5), high O unsaturated (AI_{mod} < 0.5, H/C < 1.5, O/C = 0.5-0.9), aliphatic-like (H/C = 1.5-2.0, O/C < 0.9, N = 0), peptide-like (H/C = 1.5-2.0, O/C < 0.9, N > 0), sugar-like (H/C > 2.0 or O/C ≥ 0.9), aromatics (AI_{mod} = 0.5-0.67), and condensed aromatics (AI_{mod} ≥ 0.67). It should be noted that compounds identified as “aliphatic-like”, “peptide-like”, and “sugar-like” have the molecular formulae of aliphatics, peptides, and sugars, but their actual structure may differ (Spencer et al. 2014).

The chemical characteristics of molecules were evaluated by four molecular traits, namely, H/C ratio, O/C ratio, standard Gibbs Free Energy for the half reaction of carbon oxidation (GFE) (LaRowe and Van Cappellen 2011), and AI_{mod} (Koch and Dittmar 2006, 2016), as representative of recalcitrance and oxidation state of DOM. A larger O/C ratio and lower GFE can indicate a higher degree of oxidation. GFE is associated with the oxidative degradation of organic molecules by heterotrophic organisms (LaRowe and Van Cappellen 2011), and calculated by first estimating the NOSC from the equations (LaRowe and Van Cappellen 2011):

$$NOSC = -((-Z + 4a + b - 3c - 2d + 5e - 2f) / a) + 4 \quad (1)$$

$$GFE = 60.3 - 28.5 \times NOSC \quad (2)$$

where a , b , c , d , e and f are the number of atoms of elements C, H, N, O, P and S, respectively, in a given molecule, and Z is the net charge of the molecule and equals zero when formula lists contained only the neutral forms of the measured negatively ionized molecular formulae. A lower H/C ratio and higher AI_{mod} indicate a higher recalcitrance (i.e., lower bioavailability) of DOM (Šantl-Temkiv et al. 2013, D'Andrilli et al. 2015). AI_{mod} is calculated from the equation (Koch and Dittmar 2006, 2016):

$$AI_{mod} = \frac{1 + C - \frac{1}{2}O - S - \frac{1}{2}(N + P + H)}{C - \frac{1}{2}O - N - S - P} \quad (3)$$

Development of the indicator of compositional-level thermal responses

We developed the indicator to quantify how and to what extent DOM assemblages respond to temperature change for each sample. The indicator reflects two dimensions of the compositional-level environmental responses of DOM to warming (hereafter referred to as its thermal responses, abbreviated as “iCER”): the strength and diversity of these thermal responses (termed “iCER_{avg}” and “iCER_{var}”, respectively). The indicator development was based on the direction and magnitude of each molecule’s thermal response, termed molecule-specific environmental response to temperature (MER). The input of our development procedures is the relative abundance table of each sampled DOM composition, and the outputs are the iCER_{avg} and iCER_{var} values of each sample. We described methods for each of these procedures in turn.

We randomly partitioned the whole dataset into two independent subsets by applying the common split ratio of 80:20, as first reported in Hu et al. (2024). One dataset of DOM and water temperature was used for producing MERs (termed “MER dataset”), and the remaining dataset was for $iCER_{avg}$ and $iCER_{var}$ calculations (termed “ $iCER$ dataset”). These two independent subsets ensure that the relative abundance of individual molecules would not be repeatedly used for MER and $iCER_{avg}$ (or $iCER_{var}$) calculations, and thus $iCER_{avg}$ (or $iCER_{var}$) could be further calculated from the MERs. In the current practice, 80% of all samples (that is, MER dataset) were used to calculate the MERs of individual molecules, and the remaining 20% of the samples (that is, $iCER$ dataset) were then used to calculate the $iCER_{avg}$ (or $iCER_{var}$) of each sample based on the relative abundance of individual molecules and their MERs. This data partitioning and indicator calculations were randomly performed for 999 times, and the MER and $iCER_{avg}$ (or $iCER_{var}$) were averaged across randomization for the subsequent statistical analyses. In addition, we applied the data splitting in each ocean or cruise to compare MERs among different spatial regions (see statistical analysis of “spatial transferability”).

Our procedures begin by calculating MERs for individual molecules using the MER dataset. MERs were quantified by an effect size index, i.e., the correlation coefficient ρ between the relative abundance of each molecular formula and water temperature using the Spearman’s rank correlation as described in Hu et al. (2024). Larger negative and positive Spearman ρ indicate that molecules have strong negative and positive thermal responses, respectively. To reduce Type I errors in the correlation calculations created by low-occurrence molecules, the majority rule was applied, that is, we retained molecules observed in more than 20% of samples in the MER dataset (≥ 131 samples). The 4,292 molecules were filtered and then used in subsequent analyses.

The next step in the procedures calculates $iCER_{avg}$ and $iCER_{var}$ values for each sample using $iCER$ dataset. We synthesized the MERs of all molecules into two compositional-level metrics of $iCER_{avg}$ and $iCER_{var}$. The $iCER_{avg}$ and $iCER_{var}$ were calculated as the relative abundance-weighted mean and standard deviation of MERs, respectively, using the equations:

$$iCER_{avg} = \frac{\sum(MER_i \times I_i)}{\sum(I_i)} \quad (4)$$

$$iCER_{var} = \sqrt{\frac{\sum((MER_i - iCER_{avg})^2 \times I_i)}{\sum(I_i)}} \quad (5)$$

where MER_i and I_i are the MER value and relative abundance, respectively, for each individual molecule i .

Statistical analyses

(1) Spatial transferability of molecule-specific thermal responses and their associations with molecular traits

At the molecular level, we assessed whether a given molecule showed the same MER across different spatial regions (that is, “spatial transferability”), where different environmental gradients may occur (i.e. changes in climates, salinity, and light). The degree of spatial transferability was quantified by the statistical relationships between the MERs of two sample groups across the oceans or cruises. The statistical relationships were represented by the adjusted R^2 or the slope of the linear regression. Across the oceans, we defined two sample groups based on the Atlantic and Pacific Oceans, and then examined the statistical relationships between the MERs of the two oceans for all molecules, as well as for the subsets of molecules within each category of compound classes. Across the cruises, we defined six sample groups based on the different cruises, and then examined the statistical relationships between the MERs of each pair of cruises for all molecules.

We further assessed how the molecular composition and traits (e.g., recalcitrance and oxidation state) of DOM changed towards stronger thermal responses of individual molecules. We created a continuum of thermal responses by categorizing all molecules into equal-sized bins and then examined the continuous and/or sharp transitions in molecular composition or traits along the continuum. Practically, we first separated the molecules into two groups with negative and positive MERs, and sorted the molecules of each group along thermal response gradients, that is, from the lowest to highest absolute values of MER. We categorized the molecules into 189 and 201 equal-sized

bins (200 molecules per bin) for the groups with negative and positive MERs, respectively, according to the magnitude of MER values. We then calculated the mean MERs for each of the 390 bins, resulting in a MER continuum ranging from -0.57 to 0.69. For each bin, we measured the percentage of molecular richness (that is, number of assigned peaks) for each compound class and the mean (\pm s.e) values of individual molecular traits including H/C, O/C, GFE and AI_{mod}.

(2) Depth profiles of apparent carbon concentrations of DOM molecules

We assessed how the apparent carbon concentrations for DOM molecules with negative or positive MERs changed from the surface to the deep ocean at each station. We first quantified the apparent carbon concentrations as the normalized mass peak intensities weighted by the respective SPE-DOC concentration. This calculation was performed for each molecule individually or summed in the 390 molecule bins mentioned above). The apparent carbon concentration for a molecule i (DOC _{i}) was calculated using the equation:

$$\text{DOC}_i = \text{DOC} \times I_i \quad (6)$$

where DOC is the concentration of SPE-DOC (μM) and I_i is the relative abundance of individual molecules. The apparent carbon concentration for multiple molecules (DOC _{j}) in bin j was summed across these molecules using the equation:

$$\text{DOC}_j = \sum_{i=1}^m \text{DOC}_i \quad (7)$$

where m is the number of molecules in each bin. In summary, the molecules with negative, positive, and neutral MERs accounted for 43.5-49.4%, 33.1-39.2%, and 15.7-16.6% of the total number of molecular formulae and had apparent carbon concentrations of 8.0-9.2, 5.3-8.0, and 2.6-3.2 μM , respectively, across all samples (Fig. S15). We note that this study focuses on SPE-DOC (rather than bulk DOC) because it is the analytically attainable fraction for molecular DOM characterization via FT-ICR-MS.

At each station, we then tested the statistical relationships between apparent carbon concentrations of DOM molecules and water depth using two-sided Spearman's

rank correlation. For each molecule bin, we also tested the statistical relationships between its compositional dissimilarity (Bray–Curtis) and the difference in depth using Mantel test with 999 permutations. Across the stations, we further calculated the percentages of statistically nonsignificant or significant relationships described above for individual molecules or the molecule bins.

(3) Geographical patterns of compositional-level thermal responses and their associations with DOC concentration

At the compositional level, we explored the relationships of $iCER_{avg}$ (or $iCER_{var}$) with latitude, water depth, and water temperature using linear models, and F-statistic was used to test the significance of regression. In addition, we assessed how $iCER_{avg}$ (or $iCER_{var}$) associated with the apparent carbon concentrations for all molecules along the MER continuum. Similarly, we grouped the molecules into 390 molecule bins as above. The apparent carbon concentrations of molecules summed in each bin were used and the statistical relationships were tested using the adjusted R^2 or the slope of linear models.

The above analyses were also examined across different depths, namely, 0-20, 20-40, 40-60, 60-100, 100-200, 200-300, 300-1,000, 1,000-2,000, 2,000-3,000, and >3,000 m. To concisely compare the results between the surface and deep ocean, we grouped the representative depths shallower than 200 m and deeper than 1,000 m, respectively. We provided additional support to compare the results between the surface and deep ocean based on water masses (Fig. S16, S17). We confirmed that the results were robust to the two classification methods. Specifically, samples were grouped into surface and deep ocean based on water masses following the work from Schmitz (Schmitz Jr. 1995) and Talley (Talley et al. 2011, Talley 2013) for the open ocean basins and Orsi et al. (Orsi et al. 1999) for the Southern Ocean and Antarctic water masses. Surface water masses include Subantarctic/Subarctic Surface Water (SASW; latitude > 40° N or S and latitude < 50° S, and $\sigma_\theta < 27 \text{ kg m}^{-3}$), Subtropical Surface Water (SSW; 20° < latitude < 40° N or S, and $\sigma_\theta < 27 \text{ kg m}^{-3}$), Equatorial Surface Water (EqSW; latitude between 20° N and 20° S, and $\sigma_\theta < 27 \text{ kg m}^{-3}$), and Antarctic Surface Water (AASW;

latitude > 50 S, and salinity < 34.4 and depth < 250 m). Deep water masses include North Atlantic Deep Water (NADW; $\sigma_\theta > 27.5$ kg m $^{-3}$, and $\theta > 2$ °C), Antarctic Bottom Water (AABW; $\theta < 2$ °C, and salinity > 34.5), Circumpolar Deep Water (CDW; $\theta < 2$ °C, and salinity > 34.5), and Pacific Deep Water (PDW; $0 < \text{latitude} < 40$ N, and $100 < \text{AOU} < 250$ μM).

(4) Key drivers of environmental factors and ecosystem processes underlying the compositional-level thermal responses

We further assessed the key drivers of environmental factors and ecosystem processes underlying iCER_{avg} and iCER_{var} using random forest analysis, Pearson correlation, and structural equation modelling (SEM) (Grace et al. 2012). Environmental factors included water temperature, salinity, water depth, and latitude. We considered two key ecosystem processes of microbial transformations and photodegradation, which were quantified using the indices of I_{bio} and I_{photo} , respectively (Bercovici et al. 2023c). The I_{bio} was developed based on the relative abundance of ten marker molecules of DOM derived from a three-year mesocosm experiment on DOM production by a natural microbial community of phyto- and bacterioplankton (Osterholz et al. 2015, Bercovici et al. 2023c). The I_{photo} was developed based on the relative abundance of ten marker molecules of DOM derived from a photodegradation experiment on DOM photodegradation by a solar simulator emitting high energy irradiance (Stubbins and Dittmar 2015, Bercovici et al. 2023c). High I_{bio} and low I_{photo} of a sample indicate that biological reworking and photodegradation are two important processes that shape current state of the DOM composition (Bercovici et al. 2023c).

First, random forest analysis was conducted to quantify the variations explained by environmental factors. The importance of each predictor variable was determined by evaluating the decrease in prediction accuracy (that is, increase in the mean square error between observations and out-of-bag predictions) when the data for that predictor were randomly permuted. The accuracy importance measure was estimated for each tree and averaged over the forest (2,000 trees). The relative importance of individual predictors was calculated by normalizing with the importance of the most important

predictor and then multiplying by the corresponding model performance (that is, R^2). This analysis was conducted using the R package caret V6.0.94. Second, two-sided Pearson correlation analysis was used to explore the relationships between $iCER_{avg}$ (or $iCER_{var}$) and the two ecosystem processes. Third, SEM analysis was used to explore how environmental factors influenced $iCER_{avg}$ and $iCER_{var}$ directly and indirectly through the two ecosystem processes. Before modelling, all variables in the SEMs were Z-score transformed and the more informative predictors were only retained where variables strongly correlated (Pearson correlation coefficients > 0.75). We used composite variables to account for the collective effects of environment factors, and the observed indicators for each composite variable were selected based on the multiple regressions for $iCER_{avg}$ (or $iCER_{var}$) (Table S1). The best-fitting models were reported as that with the lowest AIC value from models with a non-statistically-significant χ^2 test ($P > 0.05$), which tests whether the model structure differs from the observed data, high comparative fit index (CFI > 0.95) and low standardized root mean squared residual (SRMR < 0.05) (Table S2). We implemented the SEMs using R package lavaan V0.5.23 (Rosseel 2012), and more details on this method were described in previous literature (Hu et al. 2022).

Global mapping of compositional-level thermal responses

We estimated the spatiotemporal changes in $iCER_{avg}$ and $iCER_{var}$ across the global ocean in 1950 and 2020 by including 13 environmental predictors to a machine learning-based random forest model. We collected water depth and 12 global environmental variables (i.e., water temperature, salinity, and radiation attributes) extracted from global mapping products from 1940 to 2020. Specifically, we employed the IAP gridded monthly average temperature (Temp) and salinity with $1^\circ \times 1^\circ$ horizontal resolution at 41 vertical levels for the upper 0–2,000 m (<http://www.ocean.iap.ac.cn>). For radiation-related variables, we used surface latent heat flux (SLHF), surface sensible heat flux (SSHF), surface net long-wave (thermal) radiation (STR), and surface net short-wave (solar) radiation (SSR) from the ERA5 monthly average data with $1^\circ \times 1^\circ$ horizontal resolution

(<https://cds.climate.copernicus.eu>). The climate-related variables generally exhibit higher dynamism over time and may not directly explain the variations in DOM thermal responses at the time of sample acquisition. To reduce noise in the data, we used the long-term (e.g., 10-years) average or standard deviation of these variables for the global mapping analysis. Practically, we aggregated dynamic covariates to annual means or standard deviations over a window size of 10 years (left side, i.e., 10 years before the date of thermal response projecting). These environmental variables were chosen because they explained similar variations to those by the *in situ* measured variables, such as water temperature and salinity (Fig. S18).

We first trained the random forest model to identify the most significant variables explaining the variations in $iCER_{avg}$ and $iCER_{var}$. Before modelling, the more informative predictors were only retained where variables strongly correlated (Pearson correlation coefficients > 0.75). To fit the model, a tenfold cross-validation was conducted. Specifically, 80% of data were used to train the random forest model, and the remaining 20% to validate the model. The model performance was assessed by the rooted mean squared error (RMSE) and determination coefficient (R^2), and the best model was selected with the highest R^2 . The relative importance of each predictor variable was determined as previously described (see statistical analysis of “random forest”). The random forest model with the lowest RMSE was then applied to predict $iCER_{avg}$ (or $iCER_{var}$) in each $1^\circ \times 1^\circ$ pixel across the global ocean. The uncertainty of thermal responses was estimated as the standard error of individual predictions of 2,000 trees in the random forest model (Fig. S19). The mapping analysis was performed at 39 water depths for the upper 0–2,000 m in 1950 and 2020.

We finally estimated the impact of changes in $iCER_{var}$ from 1950 to 2020 on the changes in the concentration of recalcitrant DOC in the global ocean. The concentration of recalcitrant DOC is calculated as the apparent carbon concentrations of molecules with significantly negative MERs and divided by DOM extraction efficiency. This is because the molecules with more negative MERs were more recalcitrant and persistent, as shown in Figs. 1, 2). The estimate was based on the rate in change in the apparent carbon concentration of molecules with negative MERs with respect to $iCER_{var}$ using

the equation:

$$\text{Change in recalcitrant DOC} = \text{Slope} \times \frac{\Delta \text{iCER}_{\text{var}}}{2020-1950} \times \text{Volume} \quad (16)$$

where *Slope* is the linear slope of the relationship between the iCER_{var} and the apparent carbon concentration of molecules with negative MERs. $\Delta \text{iCER}_{\text{var}}$ is the change in iCER_{var} from 1950 to 2020. *Volume* is the volume of seawater which could be obtained from Costello et al. (2010). The concentration of recalcitrant DOC across different water depths was separately calculated at depths of < 100, 101-500, and > 1,000 m.

References

- Anderson, S. I., A. D. Barton, S. Clayton, S. Dutkiewicz, and T. A. Rynearson. 2021. Marine phytoplankton functional types exhibit diverse responses to thermal change. *Nature Communications* **12**:6413.
- Armstrong McKay, D. I., S. E. Cornell, K. Richardson, and J. Rockström. 2021. Resolving ecological feedbacks on the ocean carbon sink in Earth system models. *Earth System Dynamics* **12**:797-818.
- Arrieta, J. M., E. Mayol, R. L. Hansman, G. J. Herndl, T. Dittmar, and C. M. Duarte. 2015. Dilution limits dissolved organic carbon utilization in the deep ocean. *Science* **348**:331-333.
- Barantal, S., H. Schimann, N. Fromin, and S. Hättenschwiler. 2014. C, N and P fertilization in an Amazonian rainforest supports stoichiometric dissimilarity as a driver of litter diversity effects on decomposition. *Proceedings of the Royal Society B: Biological Sciences* **281**.
- Beaupré, S. R., and L. Aluwihare. 2010. Constraining the 2-component model of marine dissolved organic radiocarbon. *Deep Sea Research Part II: Topical Studies in Oceanography* **57**:1494-1503.
- Bendtsen, J., K. M. Hilligsøe, J. L. S. Hansen, and K. Richardson. 2015. Analysis of remineralisation, lability, temperature sensitivity and structural composition of organic matter from the upper ocean. *Progress in Oceanography* **130**:125-145.
- Bercovici, S., H. Osterholz, M. Wiemers, B. E. Noriega-Ortega, T. Dittmar, and J. Niggemann. 2023a. Dissolved organic matter molecular composition data and supporting metadata for multiple oceanographic cruises with RV SONNE (SO254, SO245, SO248) and RV POLARSTERN (PS79), Bermuda Atlantic Time-series Study and Hawaii Ocean Time-series. PANGAEA.
- Bercovici, S. K., T. Dittmar, and J. Niggemann. 2022. The detection of bacterial exometabolites in marine dissolved organic matter through ultrahigh-resolution mass spectrometry. *Limnology and Oceanography: Methods* **20**:350-360.
- Bercovici, S. K., T. Dittmar, and J. Niggemann. 2023b. Processes in the Surface Ocean Regulate Dissolved Organic Matter Distributions in the Deep. *Global Biogeochemical Cycles* **37**:e2023GB007740.
- Bercovici, S. K., M. Wiemers, T. Dittmar, and J. Niggemann. 2023c. Disentangling Biological Transformations and Photodegradation Processes from Marine Dissolved Organic Matter Composition in the Global Ocean. *Environmental Science & Technology* **57**:21145-21155.
- Breiman, L. 2001. Random Forests. *Machine Learning* **45**:5-32.
- Cory, R. M., and G. W. Kling. 2018. Interactions between sunlight and microorganisms influence dissolved organic matter degradation along the aquatic continuum. *Limnology and Oceanography Letters* **3**:102-116.
- Cory, R. M., C. P. Ward, B. C. Crump, and G. W. Kling. 2014. Sunlight controls water column processing of carbon in arctic fresh waters. *Science* **345**:925-928.
- Costello, M. J., A. Cheung, and N. De Hauwere. 2010. Surface Area and the Seabed Area, Volume, Depth, Slope, and Topographic Variation for the World's Seas, Oceans, and Countries. *Environmental Science & Technology* **44**:8821-8828.
- D'Andrilli, J., W. T. Cooper, C. M. Foreman, and A. G. Marshall. 2015. An ultrahigh-resolution mass spectrometry index to estimate natural organic matter lability. *Rapid Communications in Mass Spectrometry* **29**:2385-2401.
- Dall'Olmo, G., J. Dingle, L. Polimene, R. J. W. Brewin, and H. Claustre. 2016. Substantial energy input

725 to the mesopelagic ecosystem from the seasonal mixed-layer pump. *Nature Geoscience* **9**:820-
726 823.

727 Davidson, E. A., and I. A. Janssens. 2006. Temperature sensitivity of soil carbon decomposition and
728 feedbacks to climate change. *Nature* **440**:165-173.

729 Dittmar, T., B. Koch, N. Hertkorn, and G. Kattner. 2008. A simple and efficient method for the solid-
730 phase extraction of dissolved organic matter (SPE-DOM) from seawater. *Limnology and*
731 *Oceanography: Methods* **6**:230-235.

732 Dittmar, T., S. T. Lennartz, H. Buck-Wiese, D. A. Hansell, C. Santinelli, C. Vanni, B. Blasius, and J.-H.
733 Hehemann. 2021. Enigmatic persistence of dissolved organic matter in the ocean. *Nature*
734 *Reviews Earth & Environment* **2**:570-583.

735 Emerson, S., P. Quay, D. Karl, C. Winn, L. Tupas, and M. Landry. 1997. Experimental determination of
736 the organic carbon flux from open-ocean surface waters. *Nature* **389**:951-954.

737 Flerus, R., O. J. Lechtenfeld, B. P. Koch, S. L. McCallister, P. Schmitt-Kopplin, R. Benner, K. Kaiser,
738 and G. Kattner. 2012. A molecular perspective on the ageing of marine dissolved organic matter.
739 *Biogeosciences* **9**:1935-1955.

740 Friedlingstein, P., M. O'Sullivan, M. W. Jones, R. M. Andrew, D. C. E. Bakker, J. Hauck, P. Landschützer,
741 C. Le Quéré, I. T. Lujckx, G. P. Peters, W. Peters, J. Pongratz, C. Schwingshackl, S. Sitch, J. G.
742 Canadell, P. Ciais, R. B. Jackson, S. R. Alin, P. Anthoni, L. Barbero, N. R. Bates, M. Becker, N.
743 Bellouin, B. Decharme, L. Bopp, I. B. M. Brasika, P. Cadule, M. A. Chamberlain, N. Chandra,
744 T. T. T. Chau, F. Chevallier, L. P. Chini, M. Cronin, X. Dou, K. Enyo, W. Evans, S. Falk, R. A.
745 Feely, L. Feng, D. J. Ford, T. Gasser, J. Ghattas, T. Gkritzalis, G. Grassi, L. Gregor, N. Gruber,
746 Ö. Gürses, I. Harris, M. Hefner, J. Heinke, R. A. Houghton, G. C. Hurtt, Y. Iida, T. Ilyina, A. R.
747 Jacobson, A. Jain, T. Jarníková, A. Jersild, F. Jiang, Z. Jin, F. Joos, E. Kato, R. F. Keeling, D.
748 Kennedy, K. Klein Goldewijk, J. Knauer, J. I. Korsbakken, A. Körtzinger, X. Lan, N. Lefèvre,
749 H. Li, J. Liu, Z. Liu, L. Ma, G. Marland, N. Mayot, P. C. McGuire, G. A. McKinley, G. Meyer,
750 E. J. Morgan, D. R. Munro, S. I. Nakaoka, Y. Niwa, K. M. O'Brien, A. Olsen, A. M. Omar, T.
751 Ono, M. Paulsen, D. Pierrot, K. Pocock, B. Poulter, C. M. Powis, G. Rehder, L. Resplandy, E.
752 Robertson, C. Rödenbeck, T. M. Rosan, J. Schwinger, R. Séférian, T. L. Smallman, S. M. Smith,
753 R. Sospedra-Alfonso, Q. Sun, A. J. Sutton, C. Sweeney, S. Takao, P. P. Tans, H. Tian, B. Tilbrook,
754 H. Tsujino, F. Tubiello, G. R. van der Werf, E. van Ooijen, R. Wanninkhof, M. Watanabe, C.
755 Wimart-Rousseau, D. Yang, X. Yang, W. Yuan, X. Yue, S. Zaehle, J. Zeng, and B. Zheng. 2023.
756 Global Carbon Budget 2023. *Earth Syst. Sci. Data* **15**:5301-5369.

757 Grace, J. B., D. R. Schoolmaster Jr., G. R. Guntenspergen, A. M. Little, B. R. Mitchell, K. M. Miller, and
758 E. W. Schweiger. 2012. Guidelines for a graph-theoretic implementation of structural equation
759 modeling. *Ecosphere* **3**:art73.

760 Green, N. W., E. M. Perdue, G. R. Aiken, K. D. Butler, H. Chen, T. Dittmar, J. Niggemann, and A.
761 Stubbins. 2014. An intercomparison of three methods for the large-scale isolation of oceanic
762 dissolved organic matter. *Marine Chemistry* **161**:14-19.

763 Hansell, D., C. Carlson, D. Repeta, and R. Schlitzer. 2009. Dissolved Organic Matter in the Ocean: A
764 Controversy Stimulates New Insights. *Oceanography* **22**:202-211.

765 Hansell, D. A. 2013. Recalcitrant Dissolved Organic Carbon Fractions. *Annual Review of Marine*
766 *Science* **5**:421-445.

767 Henson, S. A., C. Laufkötter, S. Leung, S. L. C. Giering, H. I. Palevsky, and E. L. Cavan. 2022. Uncertain
768 response of ocean biological carbon export in a changing world. *Nature Geoscience* **15**:248-254.

Hu, A., M. Choi, A. J. Tanentzap, J. Liu, K.-S. Jang, J. T. Lennon, Y. Liu, J. Soininen, X. Lu, Y. Zhang, J. Shen, and J. Wang. 2022. Ecological networks of dissolved organic matter and microorganisms under global change. *Nature Communications* **13**:3600.

Hu, A., K.-S. Jang, A. J. Tanentzap, W. Zhao, J. T. Lennon, J. Liu, M. Li, J. Stegen, M. Choi, Y. Lu, X. Feng, and J. Wang. 2024. Thermal responses of dissolved organic matter under global change. *Nature Communications* **15**:576.

Jiao, N., G. J. Herndl, D. A. Hansell, R. Benner, G. Kattner, S. W. Wilhelm, D. L. Kirchman, M. G. Weinbauer, T. Luo, F. Chen, and F. Azam. 2010. Microbial production of recalcitrant dissolved organic matter: long-term carbon storage in the global ocean. *Nat Rev Microbiol* **8**:593-599.

Jiao, N., T. Luo, Q. Chen, Z. Zhao, X. Xiao, J. Liu, Z. Jian, S. Xie, H. Thomas, G. J. Herndl, R. Benner, M. Gonsior, F. Chen, W.-J. Cai, and C. Robinson. 2024. The microbial carbon pump and climate change. *Nature Reviews Microbiology*.

Kim, S., R. W. Kramer, and P. G. Hatcher. 2003. Graphical Method for Analysis of Ultrahigh-Resolution Broadband Mass Spectra of Natural Organic Matter, the Van Krevelen Diagram. *Analytical Chemistry* **75**:5336-5344.

Koch, B. P., and T. Dittmar. 2006. From mass to structure: an aromaticity index for high-resolution mass data of natural organic matter. *Rapid Communications in Mass Spectrometry* **20**:926-932.

Koch, B. P., and T. Dittmar. 2016. From mass to structure: an aromaticity index for high-resolution mass data of natural organic matter. *Rapid Communications in Mass Spectrometry* **30**:250-250.

LaRowe, D. E., and P. Van Cappellen. 2011. Degradation of natural organic matter: A thermodynamic analysis. *Geochimica et Cosmochimica Acta* **75**:2030-2042.

Lonborg, C., X. A. Alvarez-Salgado, R. T. Letscher, and D. A. Hansell. 2018. Large Stimulation of Recalcitrant Dissolved Organic Carbon Degradation by Increasing Ocean Temperatures. *Frontiers in Marine Science* **4**.

McCarthy, M. D., S. R. Beaupré, B. D. Walker, I. Voparil, T. P. Guilderson, and E. R. M. Druffel. 2011. Chemosynthetic origin of ^{14}C -depleted dissolved organic matter in a ridge-flank hydrothermal system. *Nature Geoscience* **4**:32-36.

Middelburg, J., G. Klaver, J. Nieuwenhuize, A. Wielemaker, W. Haas, T. Vlug, and J. Nat. 1996. Organic matter mineralization in intertidal sediment along an estuarine gradient. *Marine Ecology-progress Series - MAR ECOL-PROGR SER* **132**.

Mopper, K., D. J. Kieber, and A. Stubbins. 2015. Chapter 8 - Marine Photochemistry of Organic Matter: Processes and Impacts. Pages 389-450 in D. A. Hansell and C. A. Carlson, editors. *Biogeochemistry of Marine Dissolved Organic Matter (Second Edition)*. Academic Press, Boston.

Mopper, K., X. Zhou, R. J. Kieber, D. J. Kieber, R. J. Sikorski, and R. D. Jones. 1991. Photochemical degradation of dissolved organic carbon and its impact on the oceanic carbon cycle. *Nature* **353**:60-62.

Orsi, A. H., G. C. Johnson, and J. L. Bullister. 1999. Circulation, mixing, and production of Antarctic Bottom Water. *Progress in Oceanography* **43**:55-109.

Osterholz, H., J. Niggemann, H.-A. Giebel, M. Simon, and T. Dittmar. 2015. Inefficient microbial production of refractory dissolved organic matter in the ocean. *Nature Communications* **6**:7422.

Peltier, W. R., Y. Liu, and J. W. Crowley. 2007. Snowball Earth prevention by dissolved organic carbon remineralization. *Nature* **450**:813-818.

Pickett, S. T. A. 1989. Space-for-Time Substitution as an Alternative to Long-Term Studies. Pages 110-

- 135 in G. E. Likens, editor. Long-Term Studies in Ecology: Approaches and Alternatives.
Springer New York, New York, NY.
- Regnier, P., L. Resplandy, R. G. Najjar, and P. Ciais. 2022. The land-to-ocean loops of the global carbon
cycle. *Nature* **603**:401-410.
- Roshan, S., and T. DeVries. 2017. Efficient dissolved organic carbon production and export in the
oligotrophic ocean. *Nature Communications* **8**:2036.
- Rosseel, Y. 2012. lavaan: An R Package for Structural Equation Modeling. *Journal of Statistical Software*
48:1-36.
- Šantl-Temkiv, T., K. Finster, T. Dittmar, B. M. Hansen, R. Thyrhaug, N. W. Nielsen, and U. G. Karlson.
2013. Hailstones: A Window into the Microbial and Chemical Inventory of a Storm Cloud. *PLoS*
ONE **8**:e53550.
- Schlitzer, R. 2004. Export Production in the Equatorial and North Pacific Derived from Dissolved
Oxygen, Nutrient and Carbon Data. *Journal of Oceanography* **60**:53-62.
- Schmitz Jr., W. J. 1995. On the interbasin-scale thermohaline circulation. *Reviews of Geophysics* **33**:151-
173.
- Sexton, P. F., R. D. Norris, P. A. Wilson, H. Pälike, T. Westerhold, U. Röhl, C. T. Bolton, and S. Gibbs.
2011. Eocene global warming events driven by ventilation of oceanic dissolved organic carbon.
Nature **471**:349-352.
- Sofianos, S. S., and W. E. Johns. 2007. Observations of the summer Red Sea circulation. *Journal of*
Geophysical Research: Oceans **112**.
- Spencer, R. G. M., W. Guo, P. A. Raymond, T. Dittmar, E. Hood, J. Fellman, and A. Stubbins. 2014.
Source and biolability of ancient dissolved organic matter in glacier and lake ecosystems on the
Tibetan Plateau. *Geochimica et Cosmochimica Acta* **142**:64-74.
- Stubbins, A., and T. Dittmar. 2015. Illuminating the deep: Molecular signatures of photochemical
alteration of dissolved organic matter from North Atlantic Deep Water. *Marine Chemistry*
177:318-324.
- Talley, L. 2013. Closure of the Global Overturning Circulation Through the Indian, Pacific, and Southern
Oceans: Schematics and Transports. *Oceanography* **26**:80-97.
- Talley, L. D., G. L. Pickard, W. J. Emery, and J. H. Swift. 2011. Descriptive Physical Oceanography An
Introduction. Pages 1-6 in L. D. Talley, G. L. Pickard, W. J. Emery, and J. H. Swift, editors.
Descriptive Physical Oceanography (Sixth Edition). Academic Press, Boston.
- Toseland, A., S. J. Daines, J. R. Clark, A. Kirkham, J. Strauss, C. Uhlig, T. M. Lenton, K. Valentin, G. A.
Pearson, V. Moulton, and T. Mock. 2013. The impact of temperature on marine phytoplankton
resource allocation and metabolism. *Nature Climate Change* **3**:979-984.
- Vos, V. C. A., J. van Ruijven, M. P. Berg, E. T. H. M. Peeters, and F. Berendse. 2013. Leaf litter quality
drives litter mixing effects through complementary resource use among detritivores. *Oecologia*
173:269-280.
- Wagner, S., F. Schubotz, K. Kaiser, C. Hallmann, H. Waska, P. E. Rossel, R. Hansman, M. Elvert, J. J.
Middelburg, A. Engel, T. M. Blattmann, T. S. Catalá, S. T. Lennartz, G. V. Gomez-Saez, S.
Pantoja-Gutiérrez, R. Bao, and V. Galy. 2020. Soothsaying DOM: A Current Perspective on the
Future of Oceanic Dissolved Organic Carbon. *Frontiers in Marine Science* **7**.
- Wohlers, J., A. Engel, E. Zoellner, P. Breithaupt, K. Juergens, H.-G. Hoppe, U. Sommer, and U. Riebesell.
2009. Changes in biogenic carbon flow in response to sea surface warming. *Proceedings of the*
National Academy of Sciences of the United States of America **106**:7067-7072.

857 Yvon-Durocher, G., J. M. Caffrey, A. Cescatti, M. Dossena, P. del Giorgio, J. M. Gasol, J. M. Montoya,
858 J. Pumpanen, P. A. Stachr, M. Trimmer, G. Woodward, and A. P. Allen. 2012. Reconciling the
859 temperature dependence of respiration across timescales and ecosystem types. *Nature* **487**:472-
860 476.

861 Zakem, E. J., B. B. Cael, and N. M. Levine. 2021. A unified theory for organic matter accumulation. *Proc*
862 *Natl Acad Sci U S A* **118**:e2016896118.

863

864

865

Acknowledgements

We gratefully acknowledge the scientific party and crew for cruises ANT28-2, 4, and 5, and SO245, SO248, and SO254, BATS, and HOTS. We thank Beatriz Noriega Ortega for sample collection on cruises SO248 and SO254. We also acknowledge Aron Stubbins, Natasha McDonald, and John Casey for the HOTS and BATS sample collection. We thank Katrin Klaproth, Matthias Friebe, Melina Knoke, and Ina Ulber for lab assistance and technical support with FT-ICR-MS. We appreciate Cunjie Zhang, Shushi Peng, Gangsheng Wang, Xiancai Lu, Jutta Niggemann, Thorsten Dittmar, and Guoping Zhao for kind supports and comments. This study was supported by National Natural Science Foundation of China (42225708, 92251304, 42377122), Global Ocean Negative Carbon Emissions (Global ONCE) Program, Key Laboratory of Lake and Watershed Science for Water Security (NKL2023-QN04), and Science and Technology Planning Project of NIGLAS (NIGLAS2022GS09).

Figure legends

Figure 1. Molecule-specific thermal responses (MER) of oceanic DOM and their associations with molecular traits. (a) The distribution of MERs for DOM molecules of the samples in the Atlantic Ocean (including the Southern Ocean; yellow), the Pacific Ocean (green), and all oceans (black). n is the number of molecules with MERs that occurred in the Atlantic Ocean or the Pacific Ocean or both. (b) The spatial transferability of MERs for DOM molecules between the Atlantic and Pacific Oceans for all molecules (black line) and the subsets of molecules within each category of compound classes (colored lines). The spatial transferability was evaluated by the adjusted R^2 and slope of the linear regression of MERs between the two oceans. Statistical significance of the model fits with one-sided F-statistics is indicated by solid ($P \leq 0.05$) or dotted ($P > 0.05$) lines. Dashed line marks 1:1 relationship. We further plotted the percentage of molecular richness (i.e., number of formulae) for each (c) compound class and (d) means \pm s.e molecular traits along the continuum of negative (blue) to positive (red) MERs grouped into 390 equal-sized bins (i.e., 200 molecules per bin). The line and area colors from grey to red in (b) and (c) represent the compound classes with decreasing H/C ratios. In (d), we considered molecular traits, namely, H/C ratio, O/C ratio, Gibbs free energy (GFE), and the modified aromaticity index (AI_{mod}), as representative of recalcitrance and oxidation state of DOM. Blue and red dashed lines in (d) highlight the cutoff of 100% statistically significantly negative and positive MERs for the molecules in each bin, respectively. We showed an example in (e) to display the distribution of molecules with the continuum of negative (blue) to positive (red) MERs in van Krevelen diagrams. Specifically, the molecules are from eight representative MER bins, including neutral MERs and significant MERs ranging < 0.4 , $[-0.4, -0.2)$, $[-0.2, 0)$, $(0, 0.2)$, $[0.2, 0.4)$, and ≥ 0.4 .

Figure 2. Concentration-depth profiles for oceanic DOM molecules with negative or positive molecule-specific thermal responses (MER). (a) Conceptual illustration of how apparent carbon concentrations may change for individual molecules with negative (blue) or positive (red) MERs from the surface to the deep ocean. The

size of the pie charts indicates bulk DOC concentration. In each pie, four molecules are illustrated for simplicity and are each indicated by different sections for molecules with negative (blue) or positive (red) MERs. Empirical apparent carbon concentration-depth profiles are illustrated for two representative molecules with (b) negative and (c) positive MERs at five stations. These molecules had (b) $m/z = 391.06707$ and $MER = -0.56$ and (c) $m/z = 317.1241825$ and $MER = 0.81$. Curves were estimated with generalized additive models with $k = 5$. The relationships between the apparent carbon concentrations of molecules and water depth were further assessed along the continuum of negative (blue) to positive (red) MERs at each station, and the percentages of non-statistically significant correlations across the stations were shown in (d-f). We considered the relationships between apparent carbon concentrations and water depth for (d) each molecule individually and summed in (e) 390 bins as in Figure 1. For each molecule bin, we examined the association between the apparent carbon concentration and water depth (e), and the relationships between its compositional dissimilarity (Bray–Curtis) and the difference in depth (f). Statistical significance of the relationships in (d) and (e) was tested with the two-sided Spearman’s rank correlation, and in (f) with a Mantel test with 999 permutations. Grey dots denote molecules with the neutral MERs, while blue and red dots indicate negative and positive MERs, respectively. Blue and red dashed lines in (e) and (f) highlight the cutoff of 100% statistically significantly negative and positive MERs for the molecules in each bin, respectively.

Figure 3. The compositional-level thermal responses of oceanic DOM along geographic and temperature gradients. We plotted the strength ($iCER_{avg}$; a, c, e) and diversity ($iCER_{var}$; b, d, f) of thermal responses in DOM assemblages against absolute latitude (a, b), water depth (c, d), and water temperature (e, f) for all DOM samples (black lines, $n = 821$). For latitude and temperature, we further considered samples in two depth categories of ≤ 200 m (red lines, $n = 523$) and $> 1,000$ m (blue lines, $n = 159$). Statistical significance of linear model fits with one-sided F-statistics is indicated by solid ($P \leq 0.05$) or dotted ($P > 0.05$) lines.

Figure 4. The compositional-level thermal responses of oceanic DOM

associated with DOC concentrations (a-d) and underlying ecosystem processes (e-

h). We plotted SPE-DOC concentration against (a) $iCER_{avg}$ and (c) $iCER_{var}$ for all

samples (black lines), and samples at depths of ≤ 200 m (red lines) and $> 1,000$ m (blue

lines). Statistical significance of linear model fits with one-sided F-statistics is indicated

by solid ($P \leq 0.05$) or dotted ($P > 0.05$) lines. We also assessed the association between

(b) $iCER_{avg}$ or (d) $iCER_{var}$ and the apparent carbon concentrations of molecules,

summed across 390 bins along the continuum of molecule-specific thermal responses

(MER) as in Figure 2. We then plotted the linear slope of this association against mean

MERs for all samples (grey dots), and samples at depths of ≤ 200 m (light blue/red dots)

and $> 1,000$ m (dark blue/red dots). Dot sizes indicate adjusted R^2 of the linear models

for each bin, and the dot transparency indicates statistical significance, that is, low

transparency for significant ($P < 0.05$) and high transparency for non-significant ($P >$

0.05) models. (e-h) We further assessed the importance of microbial transformations

(I_{bio}) and photochemical degradation (I_{photo}) in explaining variation in $iCER_{avg}$ and

$iCER_{var}$. Changes in (e) $iCER_{avg}$ and (g) $iCER_{var}$ against I_{bio} or I_{photo} were shown for all

samples (black lines), and samples at depths of ≤ 200 m (red lines) and $> 1,000$ m (blue

lines). Statistical significance of linear model fits with one-sided F-statistics was

indicated by solid ($P \leq 0.05$) or dotted ($P > 0.05$) lines. Best-fitting structural equation

models illustrate the indirect effects of environmental factors (Envi, see Table S1 for

description) on (f) $iCER_{avg}$ and (h) $iCER_{var}$ mediated through I_{bio} and I_{photo} . R^2 denotes

the proportion of variance explained for the endogenous variables. Dotted and solid

arrows indicate negative and positive relationships, respectively. Arrow widths and

accompanying numbers in black are the relative effects (that is, standardized path

coefficients) of modeled relationships for all samples. Numbers in red and blue are the

standardized path coefficients for the samples at depths of ≤ 200 m and $> 1,000$ m,

respectively. The arrows in parentheses describe the modelled causal relationships, and

asterisks represent statistically significant effects at *** $P \leq 0.001$; ** $P \leq 0.01$; * $P \leq 0.05$.

Details of model fit are in Table S2.

Figure 5. Thermal responses of DOM mapped across the global ocean and

their changes since 1950. The relative importance of environmental variables in influencing (a) $iCER_{avg}$ and (b) $iCER_{var}$ was estimated by random forest models. Abbreviations of explanatory environmental variables are given in Methods, and the 10-year means and standard deviations of these variables are shown without suffix and with suffix of ‘.var’, respectively. Insets show the performance of the random forest model, with root mean squared error (RMSE) and coefficient of determination (R^2) for $iCER_{avg}$ (0.024 and 0.70, respectively) and for $iCER_{var}$ (0.006 and 0.62, respectively). Geographic distribution of (c) $iCER_{avg}$ and (d) $iCER_{var}$ in 2020 for four water depths representative of the surface, deep chlorophyll maximum, mesopelagic, and bathypelagic waters at 5, 60, 200, and 1,000 m, respectively. Left panels show global maps of modelled values at 1° spatial resolution and the right panels show latitudinal trends in mean values. Uncertainties in the mapped thermal responses are presented in Fig. S19. Vertical distributions of global mean (e) $iCER_{avg}$ and (f) $iCER_{var}$ and the of percentage change in global mean (g) $iCER_{avg}$ and (h) $iCER_{var}$ between 1950 and 2020. Dark red line indicates global means and shading denotes their standard deviations. In (e-f), the light red lines on the left and right denote the lowest 5% and the highest 5% of global values at each latitude, respectively. In (g-h), blue and red lines indicate decreased and increased changes, respectively.

Figure 1

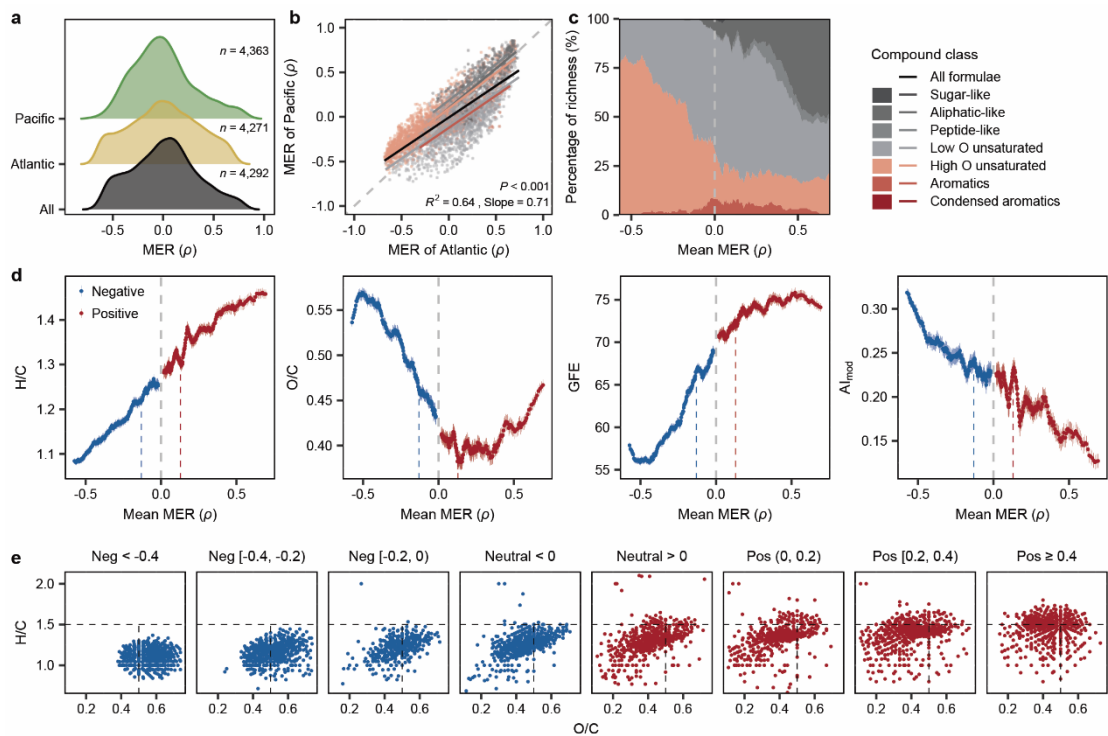


Figure 2

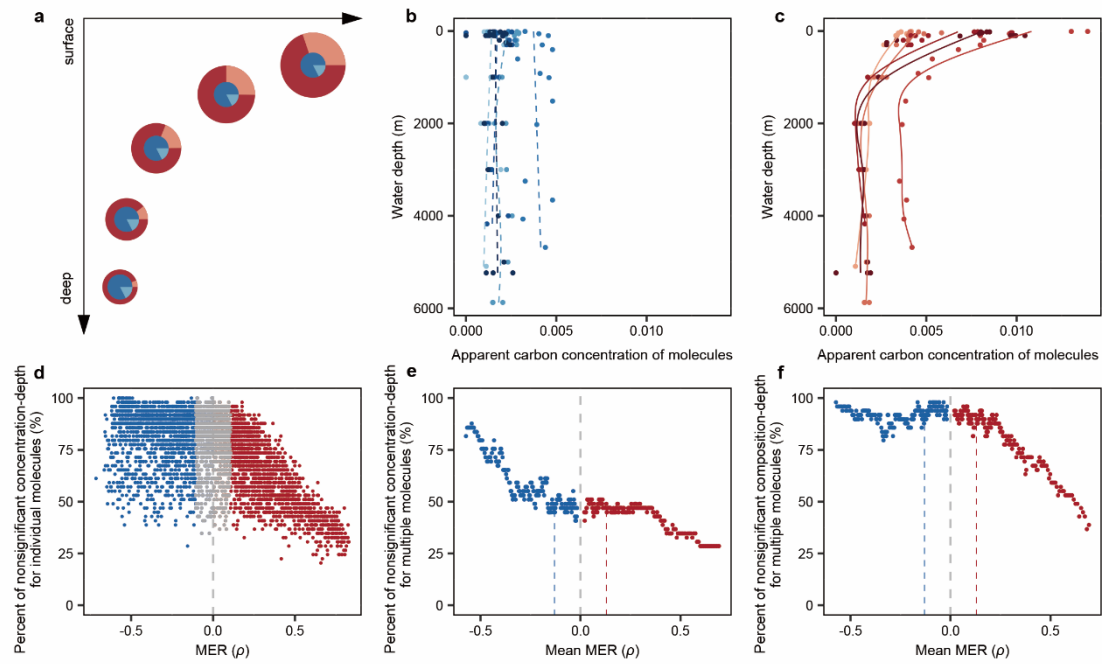


Figure 3

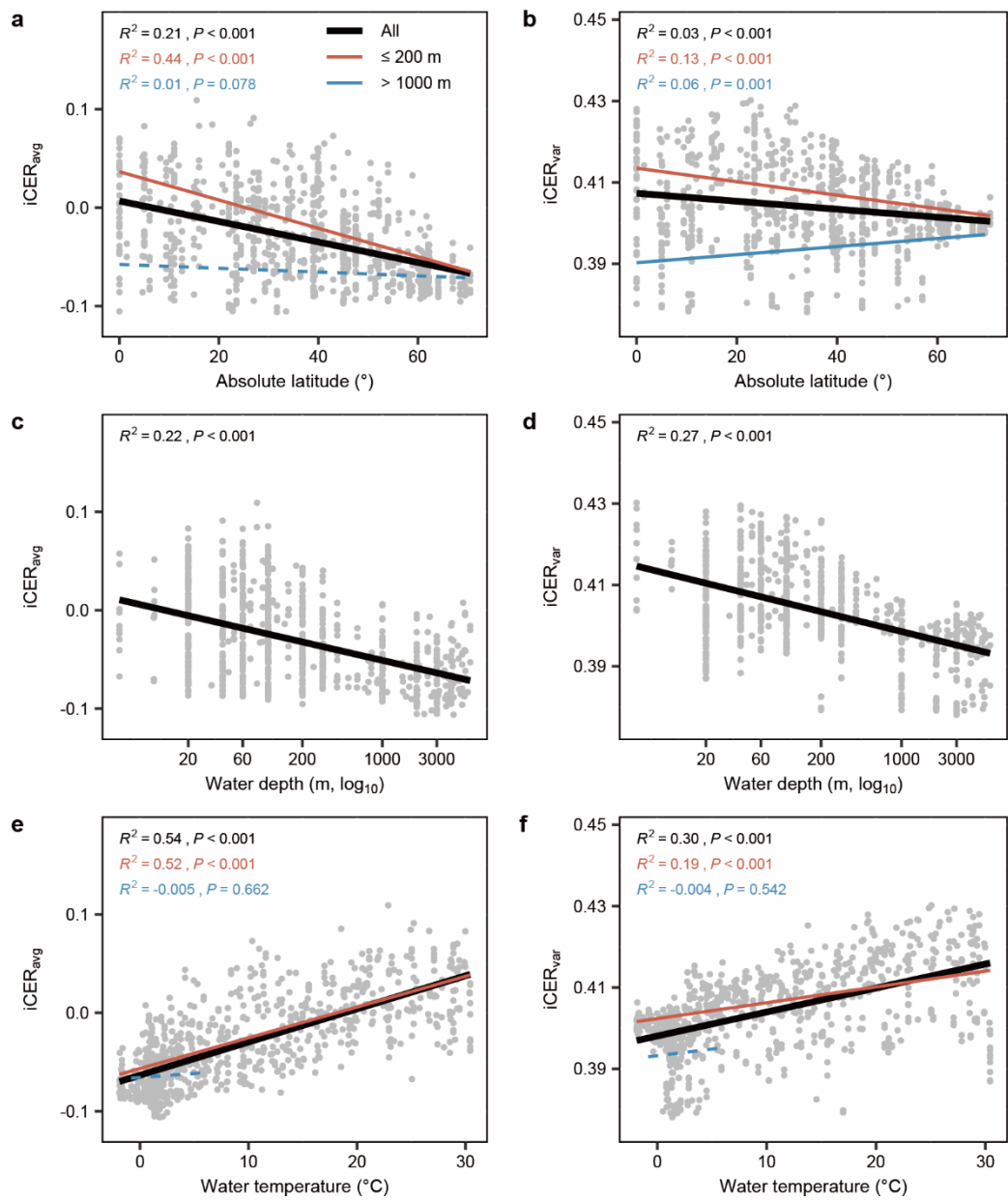


Figure 4

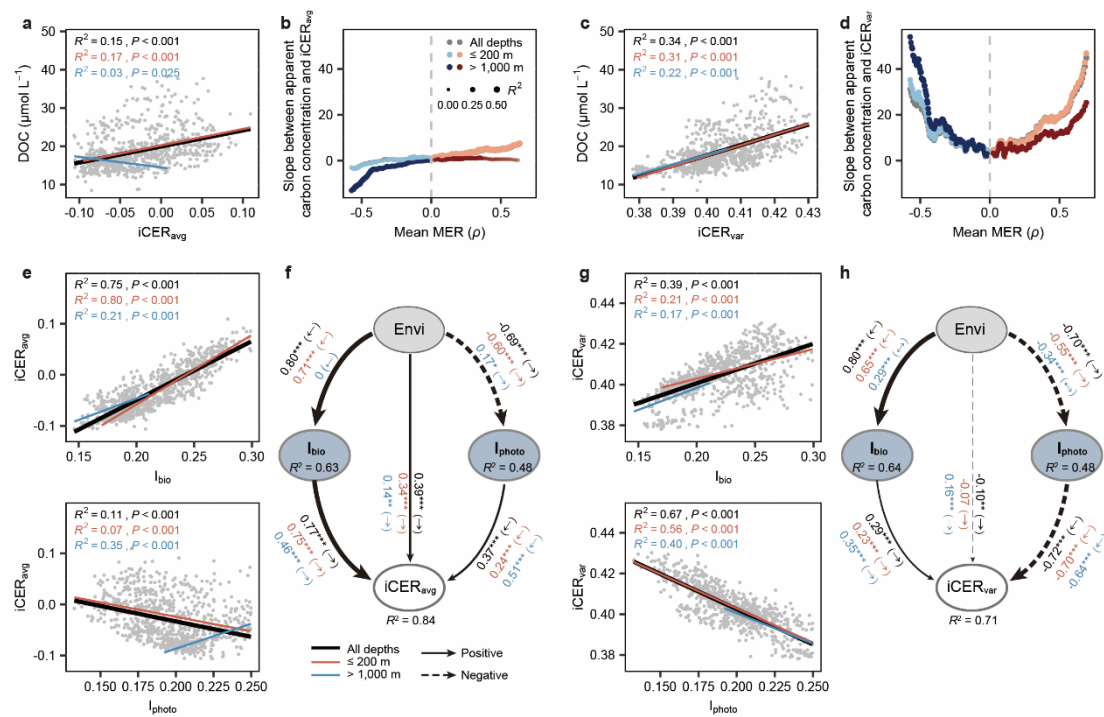


Figure 5

